Design and Characterization of a Heat-Resistant Ferritic Steel Strengthened by MX Precipitates

YAO DU, XIAOLIN LI, XU ZHANG, YIP-WAH CHUNG, DIETER ISHEIM, and SEMYON VAYNMAN

The long-term performance of current heat-resistant ferritic steels used in steam generators is primarily limited by microstructure degradation as a result of coarsening or transformation of precipitates. To improve the microstructural stability, a heat-resistant ferritic steel was designed *via* computational thermodynamics to exclusively contain metal carbonitride (MX) precipitates as the primary means for strengthening at elevated temperatures. The volume fraction of precipitates is 0.35 vol pct, about one-seventh of P91. These MX precipitates are either V-rich or Nb-rich with plate-like or spheroidal morphology, respectively. The precipitate size remains almost constant at 973 K for up to 3000 hours aging. Electron diffraction analysis revealed a Baker-Nutting orientation relationship between the precipitate and the matrix. Consistent with the thermodynamics-based design, $M_{23}C_6$-, Laves-, and Z phase were not detected. The creep threshold stress, derived from high-temperature compressive creep tests, are evaluated to be 63 ± 1 and 43 ± 2 MPa at 923 K and 973 K, respectively, on par with or slightly better than P91. This study reveals that MX precipitates in ferritic steels coarsen slowly at temperatures up to 973 K and that a relatively small volume fraction of MX precipitates can provide effective long-term creep performance at elevated temperatures.

I. INTRODUCTION

ABOUT 80 pct of the electricity generated worldwide today is produced by steam turbines. There has been a push in the past few decades to increase the operating temperature of steam generators to the ultra-supercritical (USC) regime, *i.e.*, above 873 K, for improved thermal efficiency. More advanced USC power plants target temperatures at or above 923 K.[1–4] This requires creep-resistant alloys that can operate at these temperatures for at least 100,000 hours. T/P91 and T/P92 steels are considered commercial standards for use in supercritical and USC steam generator applications. They rely on dispersion strengthening by MX precipitates, where M = (V,Nb,Ti) and X = (C,N), $M_{23}C_6$ precipitates, and Laves phase Fe_2(W,Mo) and solid-solution strengthening by W or Mo.[5–12] When exposed to these elevated temperatures for extended periods, there are concerns about microstructural degradation due to the metastability of MX, coarsening of $M_{23}C_6$ and the Laves phase, as well as Z phase formation (Cr(Nb,V)N).[13–24] In particular, the Z phase has been held responsible for the reduction of creep strength and failure of these steels after extended operation, as its precipitation results in the dissolution of finely dispersed MX.[19,25] It has been suggested that reduction of Cr and N concentration can effectively restrict Z phase formation.[23] Coarsening of $M_{23}C_6$ also causes decrease of creep strength due to the loss of effective grain boundary pinning. The coarsening resistance of MX *vs* $M_{23}C_6$ is illustrated by the work of Rojas *et al.*[26] $M_{23}C_6$ precipitates grow from 78 to 103 nm after creep deformation at 923 K for about 8000 hours, while MX precipitates start at about 30 nm and remain almost constant after the same creep deformation.

Addition of alloying elements such as W, Co, and B has been used to improve the creep properties of ferritic steels.[27–33] For example, boron addition at certain alloy compositions can stabilize $M_{23}C_6$.[27–29] Low-carbon concentrations are known to suppress or eliminate $M_{23}C_6$ formation for improved microstructural stability.[34–38] For instance, Taneike and coworkers[34]

YAO DU, YIP-WAH CHUNG, and SEMYON VAYNMAN are with the Department of Materials Science and Engineering, Northwestern University, Evanston, IL 60208. XIAOLIN LI is with the Department of Materials Science and Engineering, Northwestern University and also with State Key Laboratory of Rolling and Automation, Northeastern University, Shenyang 110819, China. XU ZHANG is with the Theoretical and Applied Mechanics Program, Northwestern University. DIETER ISHEIM is with the Department of Materials Science and Engineering, Northwestern University and also with Northwestern University Center for Atom-Probe Tomography, Northwestern University. Contact e-mail: isheim@northwestern.edu

studied the effect of C concentration and found that lower C concentration gives rise to longer rupture time. Another approach is the use of coherent B2-NiAl precipitates for improved microstructure stability.[39,40] The microstructure in this class of steels is analogous to that of γ/γ' Ni-based alloys. The hierarchical microstructure comprising of a network of B2-NiAl and $L2_1$-Ni_2TiAl[41,42] has been proved to provide more effective load transfer with less significant diffusional flow along the matrix-precipitate interface compared with single-phase B2-NiAl structure, resulting in superior creep resistance. Threshold creep strength of these steels was shown to exceed 180 MPa at 973 K.[42]

To improve the microstructural stability of heat-resistant ferritic steels, we explore the *exclusive use of semi-coherent MX precipitates* to provide the necessary creep strength at elevated temperatures, while eliminating the formation of $M_{23}C_6$, Laves phase, and Z phase. The intrinsic stability of MX precipitates and their possible pinning effect on grain and sub-grain boundaries could both contribute to the microstructural stability. The microstructure evolution and creep performance of the designed steel were studied. The steel was demonstrated to possess excellent microstructural stability and creep performance.

II. ALLOY DESIGN

Commercial thermodynamic modeling software Thermo-Calc was used with TCFE9 iron-alloy database to assist with the design of the alloy. We adopted the following design criteria: (1) existence of a fully austenitic phase field around 1273 K so as to obtain the tempered martensitic structure upon cooling, (2) thermodynamically stable precipitation of MX without $M_{23}C_6$, Laves phases, and Z phase between 923 K and 973 K, and (3) limiting the use of expensive elements such as Co. Apart from the usual C and Si additions, there are seven key elements included in this design: Cr, Mo, Nb, V, N, Mn, and Ni.

The general rule for precipitation control is to increase the concentration of alloying elements that enlarge the driving force for the formation of desirable precipitates, and reduce alloying elements that promote undesirable precipitates. Based on this principle, we limited Cr to 9 wt pct as a compromise between maintaining corrosion resistance and not promoting the formation of $M_{23}C_6$ and Z phase. Mo is generally added to provide solid-solution strengthening and to slow diffusion. In our case, we set Mo at a low level (0.13 wt pct) to minimize the driving force for the formation of $M_{23}C_6$ and Laves phase. C concentration was chosen to be 0.032 wt pct as a compromise between maximizing the volume fraction of MX and eliminating $M_{23}C_6$ in the temperature range of interest (between 923 K and 973 K). Nb concentration was set at 0.07 wt pct as in many creep-resistant ferritic steels.

Control of MX precipitation mainly relies on optimizing the concentration of MX forming elements, including V, Nb, C and N. At C concentration of 0.032 wt pct, the challenge is to produce a reasonable

MX volume fraction between 923 K and 973 K in the presence of 9 wt pct Cr. Figure 1 displays two isothermal sections of the phase diagram with varying V and N concentrations at 923 K and 973 K. While a strong carbide former, V has a high solubility in Fe, and at zero nitrogen concentration, we need V concentration in excess of 1.6 wt pct to thermodynamically stabilize MX at 923 K. By adding a small concentration of N, however, the MX phase field at 923 K enlarges, and at V concentration larger than 1.2 wt pct, MX is stable without forming $M_{23}C_6$ and Z phase, as shown in Figure 1(a). The Ferrite + MX phase field is expanded at 973 K, as the stability of $M_{23}C_6$ and Z phase decreases sharply with increasing temperature. Shaded regions in Figures 1(a) and (b) delineates the desirable composition ranges, with a thermodynamically stable MX phase and no $M_{23}C_6$ and Z phase precipitation. Here we chose V to be 1.2 wt pct and N to be 0.011 wt pct. To balance the ferrite-stabilizing elements, we adjusted Mn and Ni concentrations to ensure a reasonably broad austenite phase field around 1273 K. The target composition is listed in Table I, along with the actual measured composition.

Figure 2 shows the variation of equilibrium volume fraction of phases with respect to temperature (step diagram) using the measured composition shown in Table I. There are several notable points. First, in the target temperature range of 923 K to 973 K, $M_{23}C_6$, Z phase, and Laves phases are thermodynamically not stable; ferrite and MX are the only stable phases. Second, there is a clearly delineated austenite region between 1223 K and 1373 K, which is essential for subsequent formation of the tempered martensite microstructure upon cooling and aging. Third, there is a small volume fraction of primary MX precipitates in the austenite region. Although complete solutionizing of the MX phase cannot be accomplished by heating the steel to this temperature, the residual volume fraction of the primary MX precipitate is quite small (~ 0.06 vol pct). Fourth, the volume fraction of MX precipitates (V-rich and Nb-rich MX) between 923 K and 973 K is 0.35 vol pct. Compared with P91 steels, which contains about 2 vol pct $M_{23}C_6$, and 0.6 vol pct Z phase, the precipitate volume fraction for this alloy is about a factor of 7 smaller. This illustrates a key drawback of relying exclusively on MX precipitates for strengthening. However, since the strength increment from precipitation strengthening is roughly inversely proportional to precipitate size, a uniform distribution of fine and stable MX precipitates may more than compensate for their lower volume fraction in terms of creep performance compared with P91.

III. MATERIALS AND METHODS

A 100 g ingot was prepared by arc melting in an AM0.5 arc melter (Edmund Bühler GmbH, Germany). A prototype steel with composition of 0.032C-0.13Mo-0.19V-0.07Nb-1.21Mn-0.23Si (wt pct), designed by our group previously[43] was used as the base material. Then, pure elements (except N,
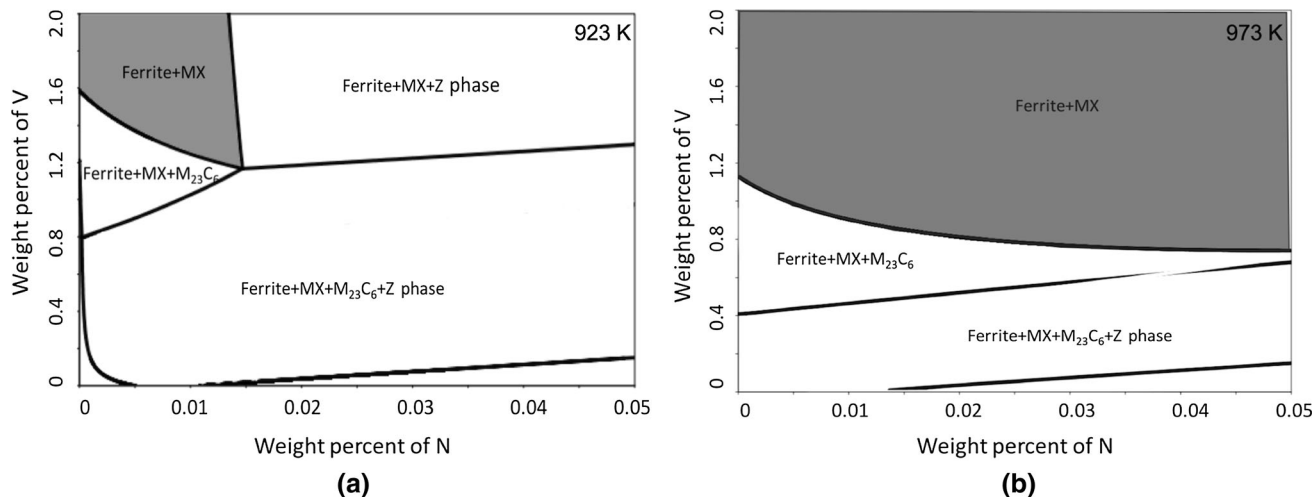
Fig. 1—Isothermal phase diagram sections at (a) 923 K and (b) 973 K with varying V and N concentrations for composition 0.032C-9Cr-0.07Nb-0.13Mo-0.23Si-1.5Mn-0.8Ni (wt pct).

Table I. Alloy Composition (Weight Percent)

	C	Cr	V	Nb	Mo	Si	Mn	Ni	N
Target Composition	0.032	9.00	1.20	0.07	0.13	0.23	1.50	0.80	0.011
Measured Composition	0.032	8.76	1.18	0.07	0.12	0.20	1.38	0.76	0.01
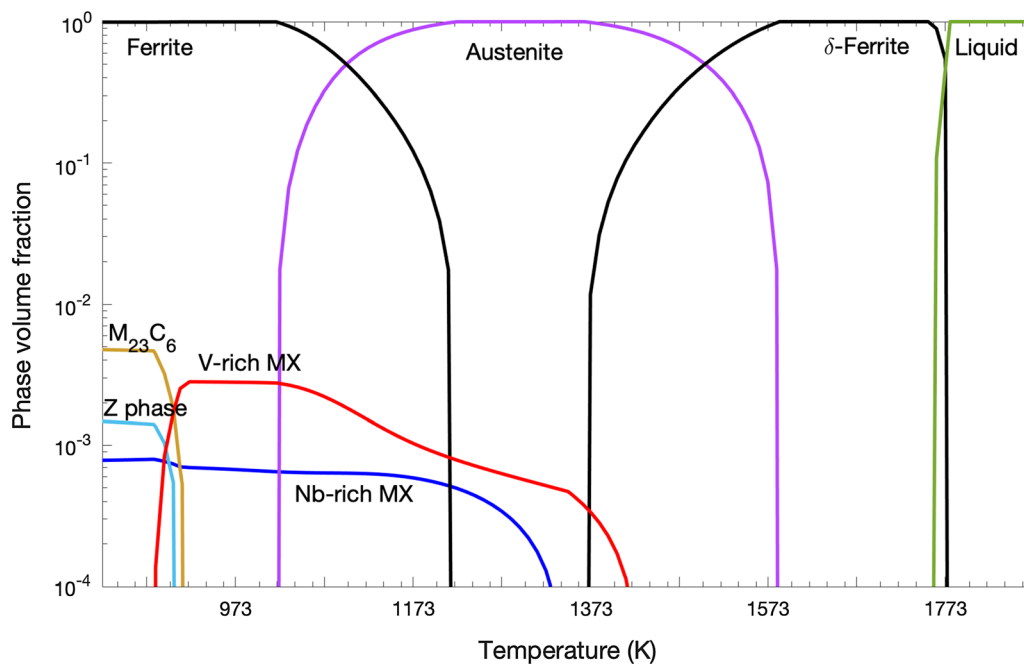
Fig. 2—Step diagram showing the variation of volume fraction of phases *vs* temperature using the measured composition shown in Table I.

introduced by adding Si_3N_4) were added to achieve the target composition. The ingot was flipped over and re-melted six times during the process for homogeneity. The composition of the ingot measured by optical emission spectroscopy was listed in Table I. The ingot was then annealed at 1273 K for 1 h in air followed by air-cooling (~ 300 K/min from 1273 K to 673 K). Room temperature tensile test was conducted using a dog-bone specimen (aged at 973 K for 10 hours, with cross-section 3 × 1 mm and gauge length 13.7 mm) with a strain rate of 0.01/min. Appropriately sized samples were cut from the ingot, and polished for

different investigations. Vickers hardness measurements at 973 K and rough vacuum (20 Pa) were performed on samples after they were aged at 973 K in air for 10 to 3000 hours. The microstructure was observed by optical and transmission electron microscopy (JEOL 2100F and JEOL ARM300F, JEOL Ltd., Japan). Polished metallographic samples were etched with Vilella's reagent (picric acid 1 g, hydrochloric acid 5 ml, ethanol 100 ml). The sample for TEM characterization was mechanically polished to a thin foil about 50 μm thick. Disks of 3 mm diameter were punched off from the thin foil and double-jet thinned (TenuPol-5, Struers Inc.), in the electrolyte consisting of 10 pct perchloric acid and 90 pct ethanol at 248 K and a voltage of 30 V. Compressive creep tests were performed at 923 K and 973 K with stepwise load increase in the range of 50 to 100 MPa. Load increase was conducted only after reaching a constant creep rate. The total strain was < 10 pct for each test. All creep specimens, with dimensions of 5 mm diameter and 10 mm length, were heated to 973 K for 10 hours before creep testing.

IV. RESULTS AND DISCUSSION

A. *Microstructure Characterization*

Figure 3 shows an optical micrograph of the steel aged at 973 K for 10 hours. The prior austenite grain size is about 300 μm. The fine martensitic features can be seen within the large grains. The TEM micrograph in Figure 4 reveals details of the martensitic lath structure and sub-grains within the lath. $M_{23}C_6$ precipitates, commonly seen on the sub-grain boundaries in conventional heat-resistant steels,[7–9] are not observed, which is consistent with the predictions of phase stability from thermodynamic modeling presented in Sect. II.

The TEM micrographs in Figure 5 reveal the nanosized precipitates in the steel after aging at 973 K for 10, 100, 1000, and 3000 hours, respectively. These precipitates nucleate and grow within sub-grains and on sub-grain boundaries. The latter precipitates can provide pinning effect similar to $M_{23}C_6$ and stabilize the
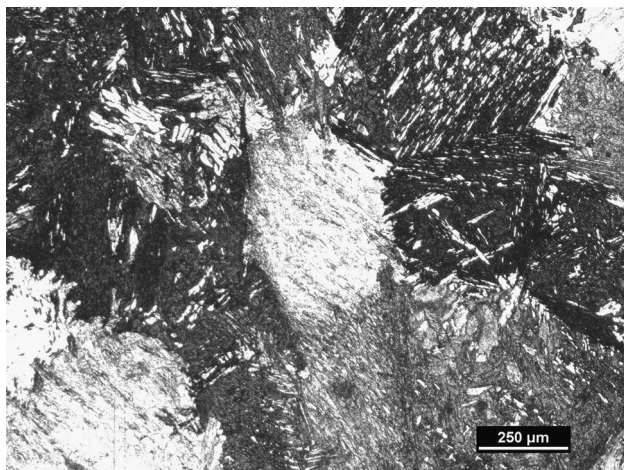
boundaries. These images indicate two precipitate morphologies: plate-like and spheroidal. Figure 6(a) is a TEM micrograph at a higher magnification. The plate-like precipitates, in particular, align in two approximately perpendicular directions, suggesting certain preferred growth orientation. Energy-dispersive X-ray measurements on the precipitates in plate-like and spheroidal shape, labeled 1 and 2 respectively, are shown in Figure 6. Discounting the unavoidable contribution from the background matrix, these spectra reveal that the plate-like precipitate is V-rich, while the spheroidal one is Nb-rich. This observation is consistent with results from thermodynamic modeling presented in Sect. II, *viz.,* the co-existence of V-rich and Nb-rich MX precipitates at 973 K. The precipitate size is estimated separately for the two types of precipitates, and described by length of the plate-like precipitates and equivalent diameter (diameter of a circle of equivalent projected area) of the spheroidal ones, as plotted in Figure 7. Each data point was obtained by averaging from about 100 plate-like and 200 spheroidal precipitates. The plate thickness cannot be determined from our TEM micrographs, due to uncertain projected orientation and strain effects on image contrast. One may conclude from these plots that these precipitates remains reasonably stable during aging at 973 K for up to 3000 hours.

Figure 8 shows a high-resolution TEM image of a plate-like precipitate and the corresponding FFT diffractogram. A Baker–Nutting relationship $(001)_{Ferrite}//(001)_{MX}$ and $[010]_{Ferrite}//[\bar{1}10]_{MX}$[44,45] can be found between the precipitate and matrix. As the diffraction spots $(110)_{MX}$ cannot be resolved from spot $(200)_{Ferrite}$, the lattice mismatch was deduced from the spot $(002)_{Ferrite}$ and $(002)_{MX}$, instead of direct measurement. The intensity profile along the diagonal was used to locate the spot center. A lattice mismatch of 2.5 ± 0.4 pct was obtained at ambient temperature, for the $(\bar{1}10)_{MX}$ planes relative to the $(020)_{Ferrite}$ planes. Figure 9 shows the selected area diffraction pattern

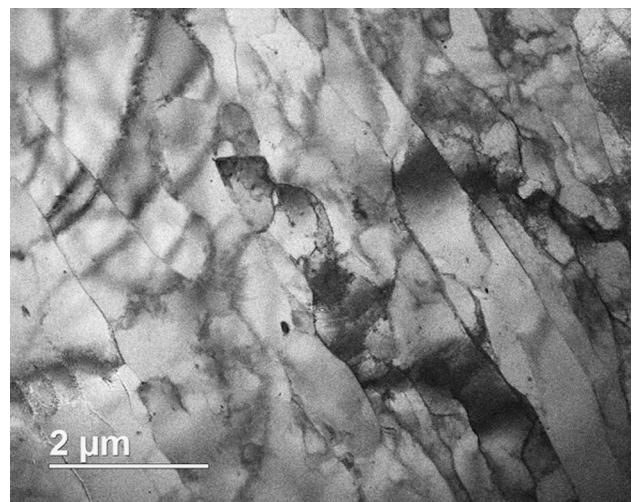Fig. 3—Optical micrograph of the steel aged at 973 K for 10 h.

Fig. 4—TEM micrograph of the steel aged at 973 K for 10 h showing the martensite lath structure.
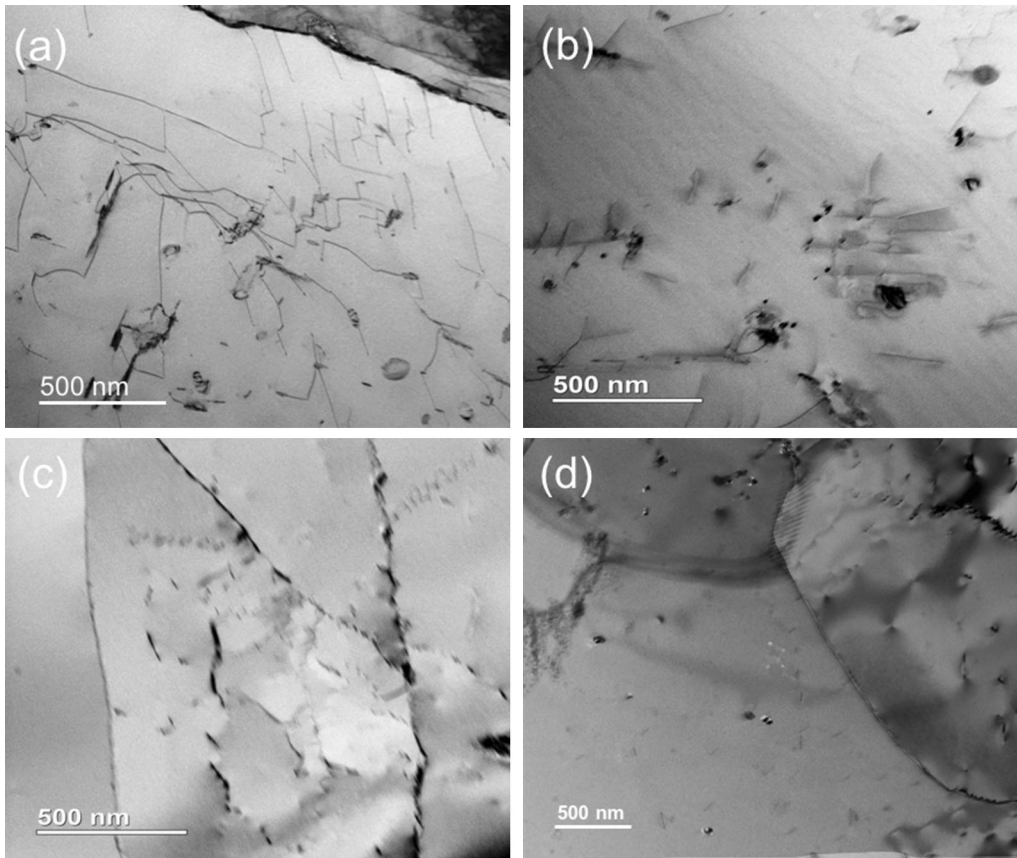
Fig. 5—TEM micrographs showing the formation of nanosized precipitates in the steel after aging at 973 K for (a) 10 h, (b) 100 h, (c) 1000 h, and (d) 3000 h.
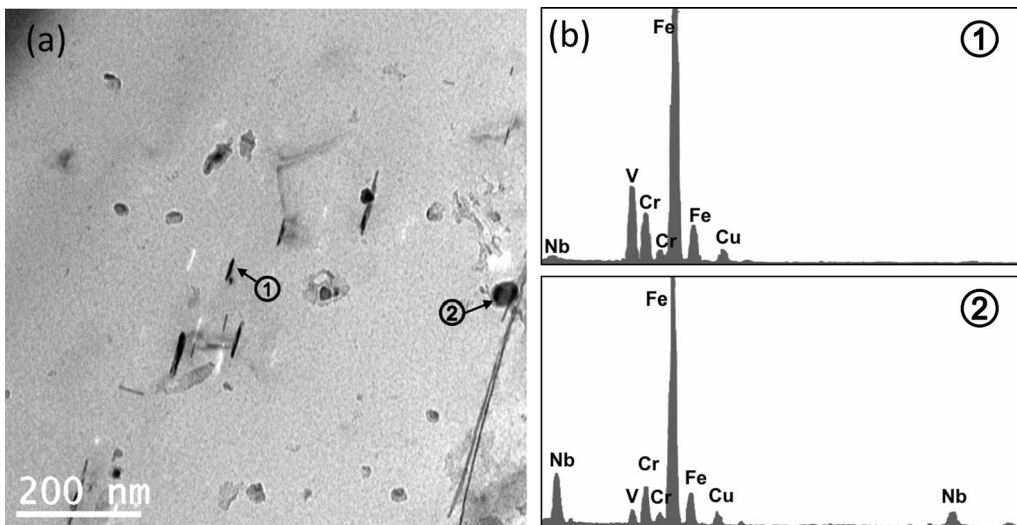

Fig. 6—(a) TEM micrograph showing the presence of plate-like (label 1) and spheroidal (label 2) precipitates after the steel was aged at 973 K for 10 h; (b) energy-dispersive X-ray spectra taken from two precipitates with label 1 and 2 in (a), showing different compositions.

from a spheroidal precipitate. It illustrates the Baker–Nutting relationship similar to the one for the plate-like precipitate shown in Figure 8. A lattice mismatch of 3 ± 0.5 pct for the $(\bar{1}10)_{MX}$ planes relative to the $(020)_{Ferrite}$ planes was determined. A lattice

mismatch of that magnitude at the given precipitate size suggests the formation of a semi-coherent interface between the precipitate and the matrix, especially for the faces of the V-rich platelet-shaped precipitates where $(\bar{1}10)_{MX}$ planes have to match up with $(020)_{Ferrite}$ planes,
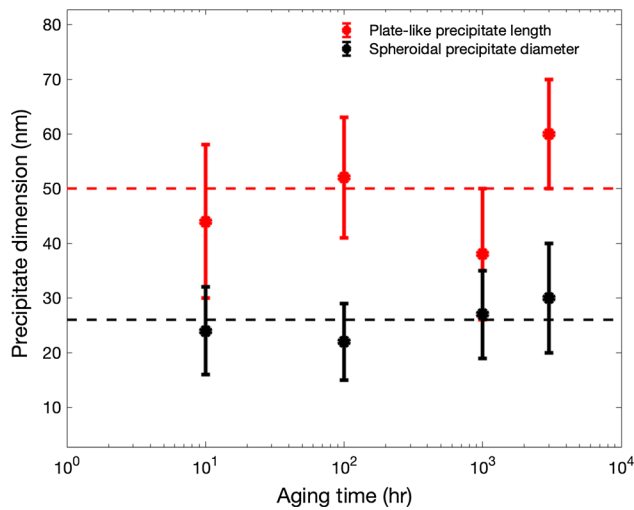
Fig. 7—Size evolution of plate-like precipitate length and spheroidal precipitate diameter *vs* aging time at 973 K. The horizontal dashed lines provide visual guidance for evaluating the thermal stability of precipitate in the course of extended aging at 973 K.

which results in lower interfacial energy, compared to a fully incoherent interface. Low interfacial energy is important to reduce the driving force for precipitate coarsening, in accordance with the LSW theory,[46,47] which predicts a direct proportionality between the coarsening rate coefficient and the interfacial energy.

B. Mechanical Properties

The room temperature yield strength, ultimate tensile strength and elongation of the steel were measured to be 310, 477 MPa and 10 pct, respectively. One would have expected higher ductility if the steel had been hot worked to eliminate the pores formed during solidification. Figure 10 shows the evolution of Vickers hardness of the steel sample measured at 973 K as a function of aging time at 973 K. It can be seen that the Vickers hardness decreases initially. The initial decrease is unlikely due to precipitate coarsening, given the stable precipitate size shown in Figure 7. Instead, the transition from martensitic to ferritic microstructure
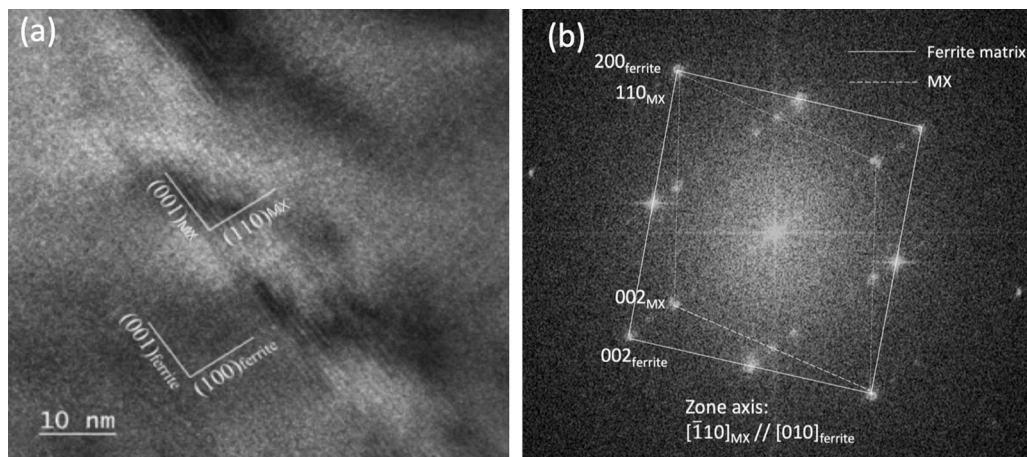

Fig. 8—(a) High-resolution TEM image of a plate-like precipitate; (b) corresponding FFT diffractogram, from a steel sample after aging at 973 K for 10 h.
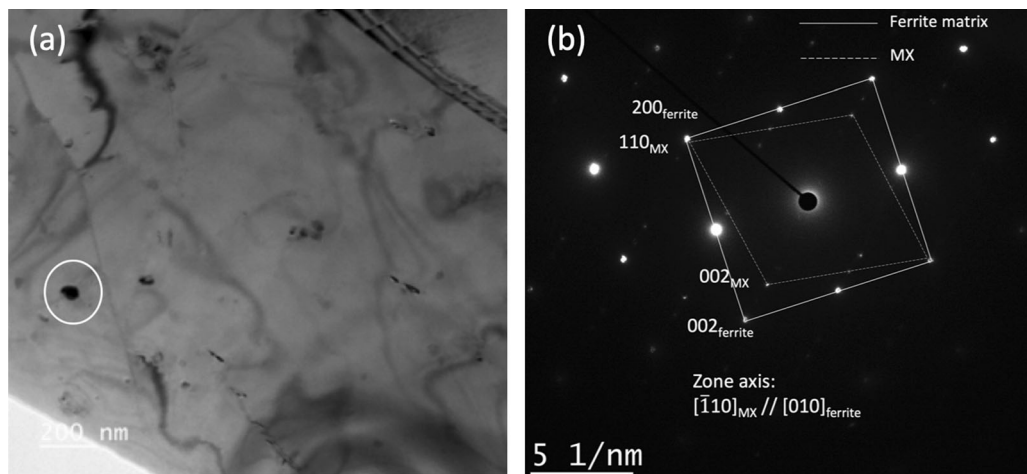

Fig. 9—(a) TEM image of a spheroidal precipitate; (b) corresponding selected area diffraction pattern, from a steel sample after aging at 973 K for 10 h.

could account for the hardness decrease, as reported by Wang et al.[38] The trend indicated by the dashed line in Figure 10 suggests that, the transition ends after aging for a few hundred hours. The hardness remains constant up to 3000 hours afterwards. It could be a rough indicator of long-term microstructure stability. It has been suggested by Dimitriu and Bhadeshia that the temperature dependence of yield strength and creep strength beyond the athermal regime are closely correlated.[48]

Figure 11(a) is a plot of the steady-state creep strain rate as a function of applied stress at 923 and 973 K. The data were obtained by measuring the creep strain as a function of time at a given applied stress. The steady-state was normally reached within 1 to 10 hours after load application, as shown in Figure 11(b). Fitting data in Figure 11(a) to a power-law equation of creep rate vs applied stress gives apparent stress exponent of 16 and 14 at 923 K and 973 K, respectively. Such large stress exponents are not consistent with any existing
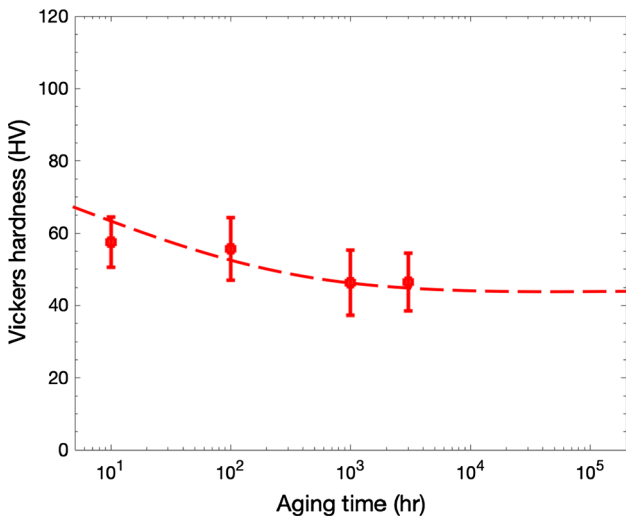
creep models. Instead, this observation suggests the existence of threshold stress that needs to be incorporated in the creep equation, defined as the stress below which the creep strain rate cannot be measured in the laboratory. The threshold stress (σ_{th}) can be introduced in a modified version of the Mukherjee–Bird–Dorn power-law creep equation as follows:

$$\dot{\varepsilon} = A \left(\frac{\sigma - \sigma_{th}}{\mu} \right)^n \exp\left(-\frac{Q}{kT} \right) \qquad [1]$$

where A is a constant, μ the shear modulus of the matrix, σ the applied stress, n the stress exponent of the matrix, Q the creep activation energy of the matrix and kT has its usual meaning.

To derive the threshold stress, we chose the matrix stress exponent $n = 4$, consistent with dislocation-mediated creep. Figure 12(a) plots $\dot{\varepsilon}^{1/4}$ of the designed steel as a function of applied stress σ for $T = 923$ K and 973 K. Extrapolation to zero strain rate gives the threshold stress of 63 ± 1 at 923 K and 43 ± 2 MPa at 973 K. Assuming A to be temperature-independent in this narrow range, we can deduce the slope of the plot in Figure 12(a) to be proportional to $\frac{1}{\mu(T)} \exp\left(-\frac{Q}{4kT} \right)$ so that the ratio of the two slopes is equal to $\frac{\mu(923K)}{\mu(973K)} \exp\left[-\frac{Q}{4k} \left(\frac{1}{973} - \frac{1}{923} \right) \right]$. From Figure 12(a), the ratio of the slope is equal to 1.57 ± 0.11. With $\frac{\mu(923K)}{\mu(973K)}$ equal to 1.04,[49] one can calculate the activation energy Q to be 246 ± 43 kJ/mole, which is close to that for the self-diffusion of bcc iron, 241 kJ/mole.[50] The same creep test was performed for P91 at 973 K, except that the P91 was forged while our designed steel was not. As shown in Figure 12(b), P91 gives a threshold stress of 35 ± 5 MPa (compression) at 973 K. As a comparison, Larson-Miller evaluation of P91 data gives a 10^5 h creep rupture strength of 26 ± 2 MPa (tension) at 973 K.[51]

The Orowan stress of the present steel can be estimated as follows:

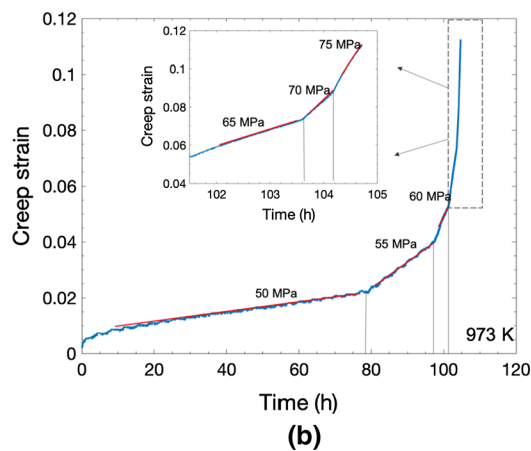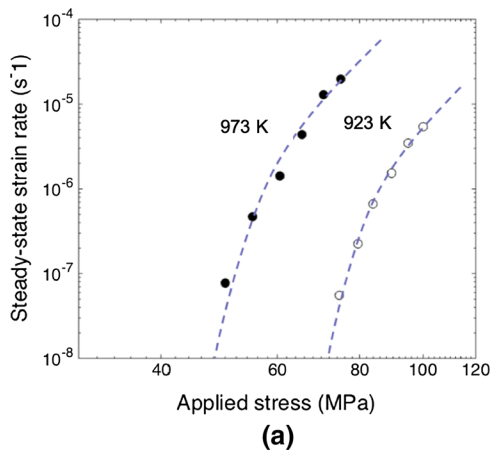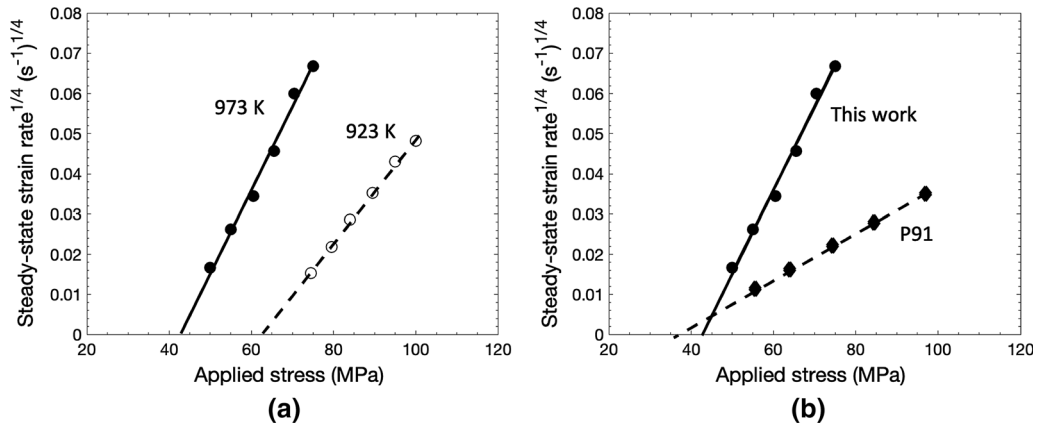Fig. 10—Evolution of Vickers hardness measured at 973 K vs aging time at 973 K.

(a)

(b)

Fig. 11—(a) Log–log plot of steady-state creep strain rate vs applied stress obtained for our steel at 923 K and 973 K; (b) plot of creep strain vs time obtained for our steel at 973 K at stepwise increasing applied stress. Each red straight line shows the regime from which we extracted the steady-state creep strain rate. The inset is a magnification of the high stress region (Color figure online).

Fig. 12—Plot of (strain rate)$^{1/4}$ vs applied stress: (a) our designed steel at 923 K and 973 K; (b) our designed steel and P91 at 973 K.

$$\sigma_{Or} = \frac{M\mu b}{\lambda} \qquad [2]$$

where M is the Taylor factor (2.9 for bcc metals), μ the shear modulus of the matrix (59.3 and 57.0 GPa at 923 K and 973 K respectively[49]), b the Burgers vector (0.248 nm), λ the edge-to-edge inter-precipitate spacing (243 nm, estimated by the formula $\lambda = \frac{d}{2}\left(\sqrt{\frac{3\pi}{4f}} - 1.64\right)$, where d is the equivalent precipitate diameter, and f the precipitate volume fraction. Calculated volume fraction, 0.35 pct, is used for the estimation. The Orowan stresses are estimated to be 176 and 169 MPa at 923 K and 973 K, respectively. Therefore, the values of σ_{th}/σ_{Or} are 0.36 at 923 K and 0.25 at 973 K.

Models for threshold stress in creep have been discussed in terms of dislocation climb over precipitates, either in the form of local climb, in which the dislocation follows closely the matrix–precipitate interface, inducing a sharp bend in the dislocation line, or general climb, in which the climb portion of the dislocation extends smoothly from the matrix–precipitate interfacial region to the glide plane.[12,52–55] The threshold stress normalized by the Orowan stress (σ_{th}/σ_{Or}) predicted by local climb is about 0.4-0.7,[56] the correct order of magnitude for reported alloys,[9,40] as well as our designed steel. However, the dislocation configuration in local climb with the sharp bend is highly unstable and is thus unlikely to occur. On the other hand, the corresponding σ_{th}/σ_{Or} ratio for general climb was predicted to be about 0.03 to 0.06,[57] not consistent with experimental findings.

Two refinements were proposed to address the shortcomings of the general climb model by incorporating attractive interaction between dislocations and incoherent precipitates[58,59] and elastic interaction between dislocations and coherent precipitates,[60,61] respectively. In the first case with incoherent precipitates, the attractive interaction is due to the reduction of dislocation line energy when the dislocation is attached to the matrix–precipitate interface, resulting in a detachment stress at the departure side of the precipitate. In the second case, with coherent precipitates, the elastic interaction comes from the stress field
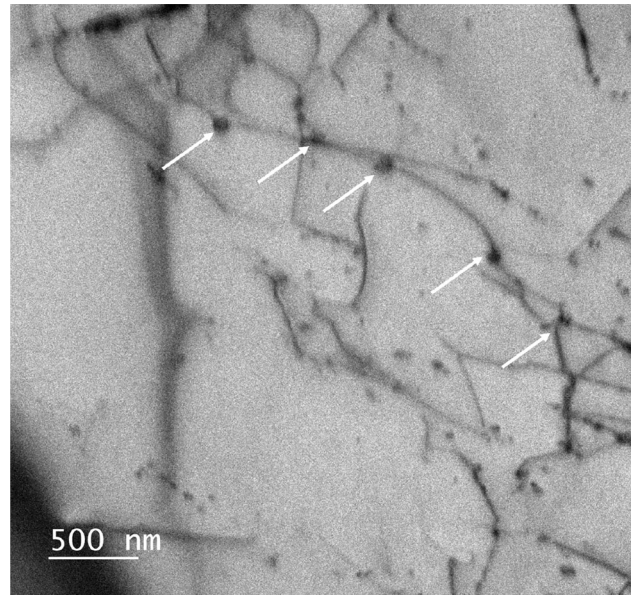

Fig. 13—TEM micrograph of the steel sample after creep testing at 973 K for 105 h with the last applied stress of 75 MPa.

of the coherent precipitate induced by the modulus and lattice misfit between the precipitate and matrix. The stress field induced by the misfitting precipitate traps the dislocation at the departure side, resulting in a threshold stress. The incorporation of either the attractive or elastic interaction to general climb brings the normalized threshold stress (σ_{th}/σ_{Or}) to the correct order of magnitude, consistent with experimental results. This model also suggests the increase of lattice parameter mismatch of precipitates to be an effective strategy to improve creep resistance.[61] The higher lattice mismatch of the MX (mainly VC) in this work might explain the slightly higher threshold stress than P91 where the MX is mainly VN. With our steel, this can be accomplished by increasing Nb concentration, although larger lattice mismatch of precipitates may result in loss of coherency, thereby accelerating precipitate coarsening.

Figure 13 displays a TEM micrograph of the precipitates and dislocations after creep testing at 973 K. The test was terminated by air-cooling with an applied stress of 75 MPa maintained. Here, we have captured the interaction between dislocations and precipitates, as indicated by the arrows. While one may not be able to discern the origin of the threshold stress from the figure, the pinning effect of the dislocation by the precipitates is demonstrated. Observations before and after creep tests show no statistically significant changes in precipitate size, demonstrating the excellent thermal stability of these MX precipitates.

V. CONCLUSION

A heat-resistant ferritic steel was designed and its microstructure and creep properties were characterized. The main results can be summarized as follows:

- The steel was designed to have MX precipitates as the primary means for strengthening; the volume fraction of these precipitates is only one-seventh of that in P91, a commercial heat-resistant steel used in power plants.
- Two types of MX precipitates are predicted by thermodynamic modeling and observed experimentally: V-rich and Nb-rich precipitates, with plate-like or spheroidal morphology, respectively. The precipitate size is almost constant during isothermal aging at 973 K up to 3000 hours.
- No $M_{23}C_6$, Laves phase, and Z phase were detected experimentally after aging at 973 K, consistent with the predictions from thermodynamic modeling.
- The creep strain rate was found to be highly stress-sensitive. The creep threshold stresses were evaluated to be 63 ± 1 and 43 ± 2 MPa at 923 K and 973 K, respectively, comparable to or slightly better than P91.

These results demonstrate the excellent microstructural stability and creep resistance of our designed steel. Our approach, which centers on the formation of thermodynamically stable MX precipitates while eliminating $M_{23}C_6$-, Laves- and Z phase, has been proved to be effective to enhance the creep strength of the steel at elevated temperatures.

REFERENCES

1. F. Masuyama: *ISIJ Int.*, 2001, vol. 41, pp. 612–25.
2. R. Viswanathan: *Adv. Mater. Process.*, 2004, vol. 162, pp. 73–76.
3. F. Abe: *Engineering*, 2015, vol. 1, pp. 211–24.
4. F. Abe, T.U. Kern, and V. Ramaswamy: *Creep-Resistant Steels*, Elsevier, Amsterdam, 2008, pp. 15–70.
5. V. Dudko, A. Belyakov, D. Molodov, and R. Kaibyshev: *Metall. Mater. Trans. A*, 2013, vol. 44A, pp. 162–72.
6. I. Fedorova, A. Kipelova, A. Belyakov, and R. Kaibyshev: *Metall. Mater. Trans. A*, 2013, vol. 44A, pp. 128–35.
7. R. Chen, H.G. Armaki, K. Maruyama, and M. Igarashi: *Mater. Sci. Eng., A*, 2011, vol. 528, pp. 4390–94.
8. M. Taneike, K. Sawada, and F. Abe: *Metall. Mater. Trans. A*, 2004, vol. 35A, pp. 1255–62.
9. T. Sakthivel, S.P. Selvi, and K. Laha: *Mater. Sci. Eng., A*, 2015, vol. 640, pp. 61–71.
10. J. Hald: *Steel Res. Int.*, 1996, vol. 67, pp. 369–74.
11. P.J. Ennis and A. Czyrska-Filemonowicz: *Sadhana*, 2003, vol. 28, pp. 709–30.
12. J. Zhao, J. Gong, A. Saboo, D.C. Dunand, and G.B. Olson: *Acta Mater.*, 2018, vol. 149, pp. 19–28.
13. K. Sawada, H. Kushima, M. Tabuchi, and K. Kimura: *Mater. Sci. Eng., A*, 2011, vol. 528, pp. 5511–18.
14. C.G. Panait, A. Zielińska-Lipiec, T. Koziel, A. Czyrska-Filemonowicz, A.F. Gourgues-Lorenzon, and W. Bendick: *Mater. Sci. Eng. A*, 2010, vol. 527, pp. 4062–69.
15. K. Maruyama, K. Sawada, and J.I. Koike: *ISIJ Int.*, 2001, vol. 41, pp. 641–53.
16. J. Hald and L. Korcakova: *ISIJ Int.*, 2003, vol. 43, pp. 420–27.
17. L. Cipolla, H.K. Danielsen, D. Venditti, P.E. Di Nunzio, J. Hald, and M.A. Somers: *Acta Mater.*, 2010, vol. 58, pp. 669–79.
18. P. Ennis, A. Zielinska-Lipiec, O. Wachter, and A. Czyrska-Filemonowicz: *Acta Mater.*, 1997, vol. 45, pp. 4901–07.
19. M. Yoshizawa, M. Igarashi, K. Moriguchi, A. Iseda, H.G. Armaki, and K. Maruyama: *Mater. Sci. Eng., A*, 2009, vol. 510, pp. 162–68.
20. K. Sawada, H. Kushima, M. Tabuchi, and K. Kimura: *Mater. Sci. Technol.*, 2014, vol. 30, pp. 12–16.
21. A. Strang and V. Vodarek: *Mater. Sci. Technol.*, 1996, vol. 12, pp. 552–56.
22. H.K. Danielsen: *Mater. Sci. Technol.*, 2016, vol. 32, pp. 126–37.
23. H.K. Danielsen and J. Hald: *VGB Powertech*, 2009, vol. 5, pp. 68–73.
24. V. Sklenička, K. Kuchařová, M. Svoboda, L. Kloc, J. Buršik, and A. Kroupa: *Mater. Charact.*, 2003, vol. 51, pp. 35–48.

25. K. Sawada, H. Kushima, and K. Kimura: *ISIJ Int.*, 2006, vol. 46, pp. 769–75.
26. D. Rojas, J. Garcia, O. Prat, G. Sauthoff, and A.R. Kaysser-Pyzalla: *Mater. Sci. Eng., A*, 2011, vol. 528, pp. 5164–76.
27. Y. Elarbi and B. Palotás: *Period. Polytech. Mech. Eng.*, 2007, vol. 51, pp. 33–38.
28. F. Abe: *Sci. Technol. Adv. Mater.*, 2008, vol. 9, p. 013002.
29. F. Liu, D.H. Fors, A. Golpayegani, H.O. Andrén, and G. Wahnström: *Metall. Mater. Trans. A*, 2012, vol. 43, p. 405362.
30. F. Abe, M. Tabuchi, H. Semba, M. Igarashi, M. Yoshizawa, N. Komai, and A. Fujita: *In 5th International Conference on Advances in Materials Technology for Fossil Power Plants*, 2007, pp. 3–5.
31. F. Abe, T. Horiuchi, M. Taneike, and K. Sawada: *Mater. Sci. Eng., A*, 2004, vol. 378, pp. 299–303.
32. J. Hald: *Trans. Indian Inst. Met.*, 2016, vol. 69, pp. 183–88.
33. P. Yan, Z. Liu, H. Bao, Y. Weng, and W. Liu: *Mater. Sci. Eng., A*, 2013, vol. 588, pp. 22–28.
34. M. Taneike, F. Abe, and K. Sawada: *Nature*, 2003, vol. 424, p. 294.
35. F. Yin and W. Jung: *Metall. Mater. Trans. A*, 2009, vol. 40A, pp. 302–09.
36. F. Yin, W. Jung, and S.H. Chung: *Scr. Mater.*, 2007, vol. 57, pp. 469–72.
37. F. Abe, M. Taneike, and K. Sawada: *Int. J. Pres. Ves. Pip*, 2007, vol. 84, pp. 3–12.
38. H. Wang, W. Yan, S. van Zwaag, Q. Shi, W. Wang, K. Yang, and Y. Shan: *Acta Mater.*, 2017, vol. 134, pp. 143–54.
39. Z. Sun, C.H. Liebscher, S. Huang, Z. Teng, G. Song, G. Wang, M. Asta, M. Rawlings, M.E. Fine, and P.K. Liaw: *Scr. Mater.*, 2013, vol. 68, pp. 384–88.
40. N.Q. Vo, C.H. Liebscher, M.J. Rawlings, M. Asta, and D.C. Dunand: *Acta Mater.*, 2014, vol. 71, pp. 89–99.
41. C.H. Liebscher, V. Radmilovic, U. Dahmen, M. Asta, and G. Ghosh: *J. Mater. Sci.*, 2013, vol. 48, pp. 2067–75.
42. G. Song, Z. Sun, L. Li, X. Xu, M. Rawlings, C.H. Liebscher, B. Clausen, J. Poplawsky, D.N. Leonard, S. Huang, and Z. Teng: *Sci. Rep.*, 2015, vol. 5, p. 16327.
43. C.T. Gross, D. Isheim, S. Vaynman, M.E. Fine, and Y.W. Chung: *Metall. Mater. Trans. A*, 2018, vol. 50, pp. 209–19.
44. H.J. Kestenbach and E.V. Morales: *Acta Microsc.*, 1998, vol. 7, pp. 22–33.
45. Z.G. Yang and M. Enomoto: *Mater. Sci. Eng., A*, 2002, vol. 332, pp. 184–92.
46. I.M. Lifshitz and V.V. Slyozov: *J. Phys. Chem. Solids*, 1961, vol. 9, pp. 35–50.
47. C. Wagner: *Z. Elektrochem., Ber. Bunsenges. Phys. Chem.*, 1961, vol. 65, pp. 581–91.
48. R.C. Dimitriu and H. Bhadeshia: *Mater. Sci. Technol.*, 2007, vol. 23, pp. 1127–31.
49. G. Ghosh and G. Olson: *Acta Mater.*, 2002, vol. 50, pp. 2655–75.
50. H.J. Frost and M.F. Ashby: *Deformation Mechanism Map*, Pergamon Press, Oxford, 1982.
51. F. Masuyama: *Int. J. Pres. Vessel. Pip.*, 2007, vol. 84, pp. 53–61.
52. R.S.W. Shewfelt and L.M. Brown: *Philos. Mag.*, 1977, vol. 35, pp. 945–62.
53. R. Lagneborg: *Scr. Metall.*, 1973, vol. 7, pp. 605–13.
54. R. Lagneborg and B. Bergman: *Met. Sci.*, 1976, vol. 10, pp. 20–28.
55. M.E. Kassner: *Fundamentals of Creep in Metals and Alloys*, Butterworth-Heinemann, Oxford, 2015.
56. J. Rösler and E. Arzt: *Acta Metall.*, 1988, vol. 36, pp. 1043–51.
57. E. Arzt and M.F. Ashby: *Scr. Metall.*, 1982, vol. 16, pp. 1285–90.
58. E. Arzt and J. Rösler: *Acta Metall.*, 1988, vol. 36, pp. 1053–60.
59. J. Rösler and E. Arzt: *Acta Metall.*, 1990, vol. 38, pp. 671–83.
60. E.A. Marquis and D.C. Dunand: *Scr. Mater.*, 2002, vol. 47, pp. 503–08.
61. M.E. Krug and D.C. Dunand: *Acta Mater.*, 2011, vol. 59, pp. 5125–34.